Dalton Transactions

Dynamic Article Links

Cite this: *Dalton Trans.*, 2012, **41**, 4594

www.rsc.org/dalton

PAPER

Superparamagnetic $Ag@Fe_3O_4$ core–shell nanospheres: fabrication, characterization and application as reusable nanocatalysts†

Wanquan Jiang,*[a] Yufeng Zhou,[a] Yanli Zhang,[a] Shouhu Xuan[b] and Xinglong Gong*[b]

Received 1st December 2011, Accepted 13th January 2012
DOI: 10.1039/c2dt12307j

Superparamagnetic $Ag@Fe_3O_4$ nanospheres with core–shell nanostructures have been prepared by a facile one-pot method. The diameter of the as-synthesized nanospheres was about 200 nm and the core sizes were between 50 and 100 nm. By varying the concentrations, particles with tunable core size and total size are successfully achieved. Time dependent experiments were constructed to investigate the synthesis mechanism, which indicated that the present method corresponded to an Ostwald ripening progress. The BET area of the core–shell nanospheres is about 22.6 m^2/g and this result indicates that the product shows a porous character. The saturated magnetization of the superparamagnetic $Ag@Fe_3O_4$ nanospheres is 27.4 emu g^{-1} at room temperature, which enables them to be recycled from the solution by simply applying a small magnet. Due to the unique nanostructure, these particles show high performance in catalytic reduction of 4-nitrophenol and can be used as reusable nanocatalysts.

1. Introduction

Core–shell composite materials have attracted increasing interest from materials scientists because they combine the advantageous properties of both the core materials and the shell materials.[1] Due to their unique physicochemical properties and great potential applications in the areas of electronics, photonics, catalysis, biotechnology, and nanotechnology, various types of bi-functional or tri-functional core–shell materials, such as inorganic–inorganic, inorganic–polymer, polymer–polymer, *etc*., have been technically synthesized.[2–9] Among them, superparamagnetic nanocomposites with core–shell nanostructures do not retain any magnetization in the absence of a magnetic field, and thus have been widely used in magnetic resonance imaging, hyperthermia, separation and purification of biomolecules, drug delivery, and catalysis.[10–16]

The magnetic particles can be conveniently separated from the mother solutions by applying an appropriate magnetic field,[17–19] therefore, the combination of nanocatalysts together with the magnetic carriers has attracted increasing attention due to their recoverable nature.[20–22] At first, most work in this area was focused on immobilization of nanocatalysts on the surface of the magnetic support to form a core–shell nanostructure.[23–25] During the past decade, various core–shell like magnetic chemcatalytic and photocatalytic nanomaterials have been developed and the morphologies have varied from spherical,[26–28] ellipsoidal,[29,30] to hierarchical nanostructures.[31] Recently, to prevent the agglomeration and to further improve the durability of the nanocatalysts, they have usually been covered by a porous inert shell. In terms of the magnetic catalysts, Yin *et al.*[32] developed a series of simple sol–gel and surface-protected etching processes to fabricate mesoporous-silica-protected core–satellite nanocomposite catalysts, which can be ideally magnetically recycled during the catalytic reactions. Alternatively, an outer shell of mesoporous silica with perpendicularly aligned pore channels can be achieved .[33] Very recently, a magnetic photocatalyst with double hierarchical shells has also been synthesized by using a hydrothermal etching assisted crystallization method.[34] However, most of this research required the preparation of core–shell precursors, requiring multistep and complex synthetic procedures.

Ag based magnetic nanocatalysts play an important role in fine and speciality chemistry because they can catalyze various reactions such as epoxidation, reduction of dyes, *et al.*[35,36] To expand the application of this bi-functional nanocomposite, different kinds of nanostructures such as Fe_3O_4–Ag core–shell like nanoparticles, heterodimers, and core–satellite particles have been prepared, which can be applied in bio-separation, catalysis, optical limiting, two-photon fluorescence imaging and magnetic manipulation.[37–40] By varying the Fe_3O_4 cores, the size of the as-prepared Fe_3O_4–Ag nanocomposites were controlled from several nanometers to micrometers. In addition, heterodimers of Fe_3O_4 hollow nanospheres and Ag nanoparticles were also successfully achieved based on the reactions at a liquid–liquid interface.[41] However, the Ag component in most of the above products was located on the surface of the magnetic carrier, structures with an Ag core and Fe_3O_4 shell were rare. Recently, Chen and his colleagues reported the preparation of a unique Ag–Fe_3O_4 composite nanosphere, in which the interior Ag

[a]*Department of Chemistry, University of Science and Technology of China (USTC), Hefei 230026, PR China. E-mail: jiangwq@ustc.edu.cn; Fax: +86-551-3600419; Tel: +86-551-3607605*
[b]*CAS Key Laboratory of Mechanical Behavior and Design of Materials, Department of Modern Mechanics, USTC, Hefei 230027, PR China. E-mail: gongxl@ustc.edu.cn*

†Electronic supplementary information (ESI) available. See DOI: 10.1039/c2dt12307j

nanocrystals show high efficiency for the epoxidation of styrene to form styrene epoxide.[42] Therefore, there will become a pressing need for Fe_3O_4 encapsulated Ag core–shell nanocomposites, not only for fundamental interest but also for their high efficiency and facility.

Herein, superparamagnetic Ag@Fe_3O_4 core–shell nanospheres were prepared by a facile one-pot hydrothermal procedure with polyacrylamide (PAM) and sodium citrate used as surfactant, and $Fe(NO_3)_3$ and $AgNO_3$ used as ion precursors. Notably, the fabrication occurred in aqueous solution and no harmful reagent was used, which indicated a green chemical reaction. The diameter of the as-synthesized nanospheres was about 200 nm and the core sizes were between 50 and 100 nm. The influences of the concentrations and time on the final products were investigated and the formation mechanism was discussed. The core–shell nanospheres show high performance in the catalytic reduction of 4-nitrophenol (4-NP). In addition, these spheres were magnetically separable and they exhibited stable reusable catalytic properties. The porous magnetic shell allows chemical and biological molecules onto the surface of the Ag core for more applications in catalysis and biomedical fields.

2. Experimental

2.1 Materials

The chemicals used for the synthesis of the core–shell nanospheres were iron(III) nitrate nonahydrate ($Fe(NO_3)_3{\cdot}9H_2O$), trisodium citrate dihydrate ($C_6H_5O_7Na_3{\cdot}2H_2O$), urea ($CON_2H_4$), polyacrylamide (PAM) and silver nitrate ($AgNO_3$). All of the chemical reagents were analytical grade and used without further purification. Deionized water was used for all experiments.

2.2 Synthesis of core–shell Ag@Fe_3O_4 nanospheres

Core–shell Ag@Fe_3O_4 nanospheres were prepared by a one-pot hydrothermal method. In a typical synthesis, 1 mmol $Fe(NO_3)_3{\cdot}9H_2O$, 3 mmol sodium citrate ($C_6H_5O_7Na_3{\cdot}2H_2O$) and 6 mmol urea were dissolved in 15 mL distilled water. Then 0.15 g PAM was added under continuous stirring until it was dissolved totally. At last, 0.5 mmol $AgNO_3$ which was dissolved in 5 mL distilled water was dropped slowly into the former solution until it had dissolved. The solution was transferred to a 30 mL Teflon-lined autoclave. The autoclave was then sealed and maintained at 200 °C for 12 h. After the autoclave had cooled down to room temperature naturally, the black precipitation was collected by magnetic separation, washed with distilled water and absolute ethanol several times, and dried under vacuum desiccation at 50 °C overnight.

2.3 Catalytic properties of Ag@Fe_3O_4 core–shell nanospheres

0.0187, 0.0262, and 0.0370 mg mL^{-1} of solution containing core–shell Ag@Fe_3O_4 nanospheres was mixed with 4-NP and the volume of the mixture was adjusted to 30 mL with deionized water. Then 10 mL of fresh $NaBH_4$ solution was rapidly injected under constant stirring. The yellow color of the solution gradually vanished, indicating the reduction of 4-NP (c (4-NP) = 5 × 10^{-5} mol L^{-1}). The concentration of 4-NP was determined spectrophotometrically at a wavelength of 400 nm using UV/vis measurement.

Similar to the above reduction process, 0.0370 mg mL^{-1} of solution containing core–shell Ag@Fe_3O_4 nanospheres was used to catalyze 4-NP (c (4-NP) = 5 × 10^{-5} mol L^{-1}, c ($NaBH_4$) = 3.2 × 10^{-2} mol L^{-1}). After reaction for 30 min, core–shell Ag@Fe_3O_4 nanospheres were collected by using a small magnet, washed twice with deionized water, and then reused. The same procedures were repeated 5 times and the core–shell Ag@Fe_3O_4 nanocatalyst still exhibited stable catalytic activity.

2.4 Measurements and characterization

X-ray powder diffraction (XRD) patterns of the products were obtained with a Japan Rigaku DMax-γA rotation anode X-ray diffractometer equipped with graphite monochromatized Cu Kα radiation (λ = 0.154178 nm). Transmission electron microscopy (TEM) images were taken on a JEM-2011 with an accelerating voltage of 200 kV TEM. The field emission scanning electron microscope (FE-SEM, 20 kV) images were taken on a JEOL JSM-6700F SEM. X-ray photoelectron spectra (XPS) were measured on an ESCALAB 250. The UV/vis spectra were recorded using a UV-365 spectrophotometer. Infrared (IR) spectra were recorded in the wavenumber range 2000–500 cm^{-1} with a Nicolet Model 759 Fourier transform infrared (FT-IR) spectrometer using a KBr wafer. Their magnetic properties (M–H curve) were measured at room temperature on an MPMS XL magnetometer made by Quantum Design Corporation.

3. Results and discussion

3.1 Preparation and characterization of the Ag@Fe_3O_4 nanospheres with a typical core–shell nanostructure

Superparamagnetic nanospheres with Ag core and Fe_3O_4 shell were prepared in a sealed system by reduction reactions between the Ag^+, Fe^{3+} and the sodium citrate. The crystalline structure of the product was characterized by XRD and the diffraction pattern was shown in Fig. 1. The reflection planes of (220),

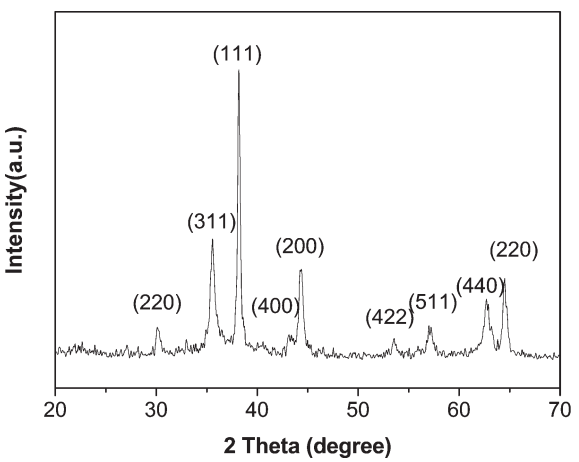

Fig. 1 XRD pattern of the as-prepared Ag@Fe_3O_4 nanospheres.

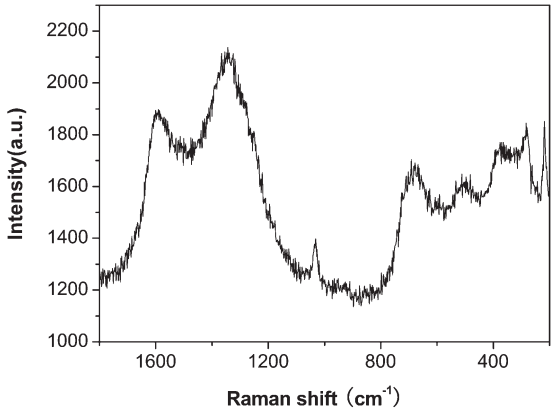

Fig. 2 Raman spectrum of the as-prepared Ag@Fe_3O_4 nanospheres.

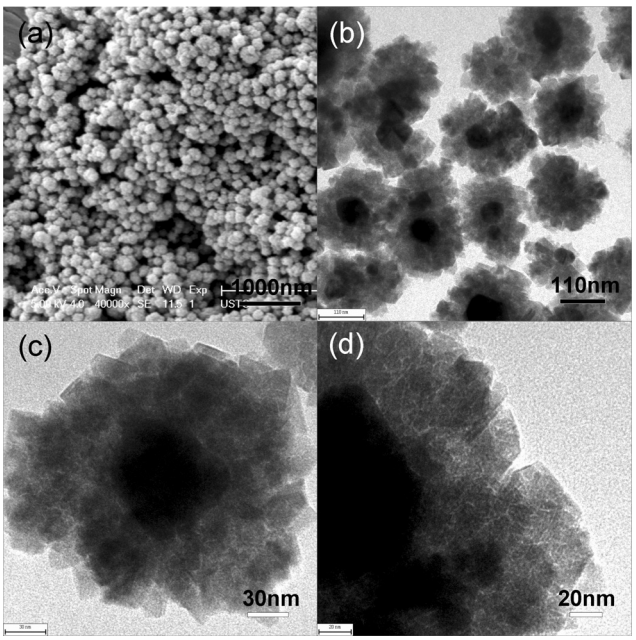

Fig. 3 SEM image (a) and TEM images (b,c,d) of the as-prepared Ag@Fe_3O_4 nanospheres.

(311), (400), (422), (511), and (440) are observed and the face-centered cubic structure of the Fe_3O_4 (JCPDS Card No. 75–0033) was identified. In addition, three peaks located at 38°, 44°, and 65° are found, which represent the Bragg reflections of the Ag ((111), (200), and (220) reflection planes (JCPDS card No. 04-0783). To further investigate the composition of the obtained product, a Raman spectrum was obtained and the spectrum is shown in Fig. 2. In this region the strongest peak at 667 cm^{-1}, which is attributed to the A_{1g} mode of Fe_3O_4, is observed. The peak at 533 cm^{-1} is the T_{2g} mode of Fe_3O_4. These two main characteristic peaks for magnetite suggest the presence of Fe_3O_4.[43] Based on the XRD and Raman analysis, it can be concluded that an Ag–Fe_3O_4 composite is successfully synthesized by using a simple one-step method.

The sizes and shapes of the samples were examined by TEM and SEM. Fig. 3a shows a representative SEM image which clearly indicates that the as-prepared Ag@Fe_3O_4 nanocomposite

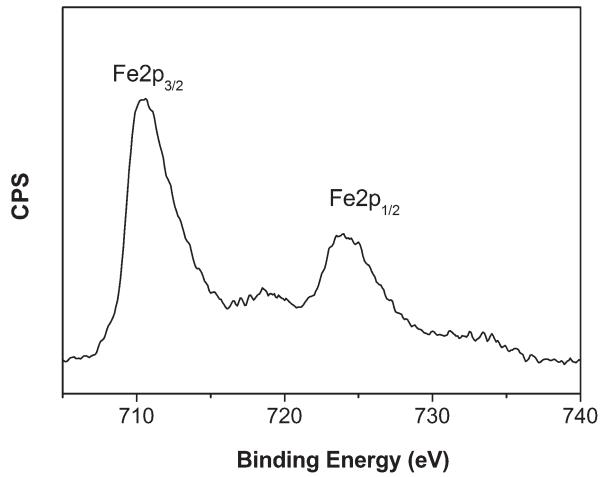

Fig. 4 High-resolution XPS spectrum of as-prepared Ag@Fe_3O_4 nanospheres between 740 and 700 eV.

shows a typical spherical nanostructure. All the particles are uniform and well dispersed on the copper grid without any large aggregations. The average diameter of the nanospheres is around 200 nm. Moreover, the surface of the particles is rough and no surface cracks and intersphere adherence are found. The well dispersed nature of the Ag@Fe_3O_4 nanospheres is also clearly demonstrated from the TEM image. As shown in Fig. 3b, the Ag@Fe_3O_4 composite nanospheres are composed of two distinct components, which demonstrates that a defined core–shell nanostructure is successfully achieved. The average diameter is about 200 nm and this agrees well with the SEM analysis. Here, the black core is the single crystal Ag and the gray shell is composed of nanosized Fe_3O_4. XPS was employed to study the surface properties of the product. Fig. 4 shows the high-resolution XPS spectrum of Ag@Fe_3O_4 nanospheres between 740 and 700 eV. The photoelectron peaks located at 711 and 725 eV correspond to the $Fe2p_{3/2}$ and $Fe2p_{1/2}$, respectively. The values are consistent with the XPS data for Fe_3O_4. In addition, the main metal signal detected by the XPS is Fe, which further indicates the as-prepared nanocomposites show an Ag core–Fe_3O_4 shell nanostructure.

Fig. 3c shows a TEM image of a typical single Ag@Fe_3O_4 nanosphere. The shape of the Ag core is irregular and the average diameter is about 50 nm. The Ag core is well wrapped by the coating shell, and the thickness of the Fe_3O_4 shell is about 70 nm. The Fe_3O_4 shell is polycrystallized and it is composed of many tiny secondary Fe_3O_4 nanocrystals. According to the Scherrer equation, the average crystallite size of the Fe_3O_4 which is calculated based on the XRD pattern is about 10 nm (Fig. 1), which agrees well with the TEM observation. A representative high resolution TEM image of the as-prepared Ag@Fe_3O_4 nanosphere is shown in Fig. 3d; it is observed that the Fe_3O_4 nanocrystals are well crystallized and they show a polyhedron-like nanostructure. Energy-dispersive X-ray spectroscopy (EDS) shows that the Ag, Fe, and O elements are present in the spectra, which indicates the formation of Ag and Fe_3O_4 (Fig. 5). The Cu and C signals in the EDS spectrum originate from the carbon-coated copper grid. These results agree well with the above analysis.

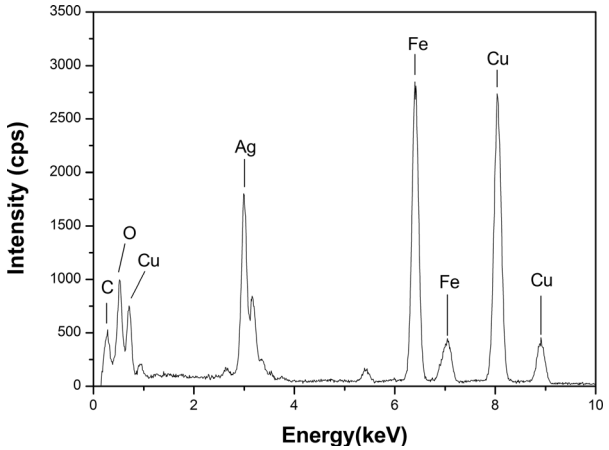

Fig. 5 EDS spectrum of as-prepared Ag@Fe_3O_4 nanospheres.

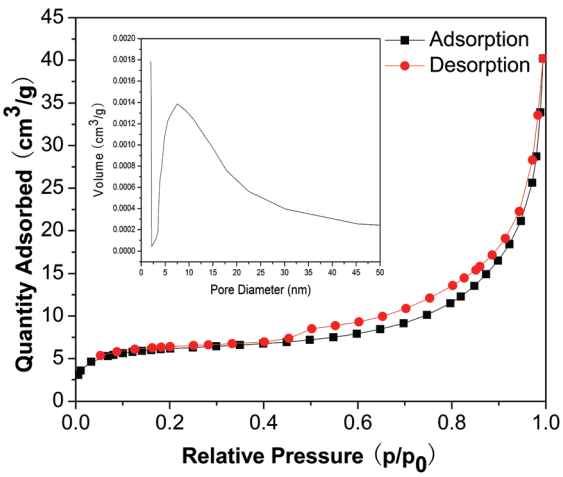

Fig. 6 Nitrogen adsorption–desorption isotherm and BJH pore plot (inset) of the as-prepared Ag@Fe_3O_4 nanospheres.

The secondary Fe_3O_4 nanocrystals exhibit a polyhedron-like shape and they are randomly packed to form a spherical shell, thus there must be a lot of interparticle and nonordered mesoporosity in the samples. In our case, the Ag nanocrystal is encapsulated by a layer of porous shell and the specific surface area of the Ag@Fe_3O_4 nanospheres was characterized using the Nitrogen adsorption–desorption technique. Fig. 6 presents the nitrogen adsorption–desorption isotherms and BJH pore size distribution curves (inset in Fig. 6). The nitrogen adsorption–desorption isotherms show typical type-IV curves, indicating the presence of interparticle and nonordered mesoporosity in the sample. In this case, the pores arise from the spaces among the nanocrystallites within a porous Fe_3O_4 shell, thus the pores are not very uniform.[44] According to the BJH pore distribution curve (inset in Fig. 6), a major pore size is found to be 7.5 nm. The BET surface area of the core–shell nanospheres is about 22.6 $m^2\ g^{-1}$, indicating the presence of mesopores in the Ag@Fe_3O_4 nanospheres, which agrees well with the TEM analysis result (Fig. 4c and d). Although the BET value is lower than the porous Fe_3O_4 micro/nanospheres,[45–47] it is higher than the value of dense spheres (8.3 $m^2\ g^{-1}$)[48] and hollow single-crystallized spheres (13.5 $m^2\ g^{-1}$).[49] Therefore, the Ag core is encapsulated by a layer of porous Fe_3O_4 shell. Because the Ag cores are solid and non-porous, the BET area of the Ag@Fe_3O_4 nanospheres is lower than the hollow Fe_3O_4 nanospheres with a porous shell. Due to the presence of the nanopores, many biomolecules and small molecular reagents can enter into the Fe_3O_4 porous shell and approach onto the surface of the Ag core, which enables this kind of core–shell particle to be widely applied in adsorption and catalysis.

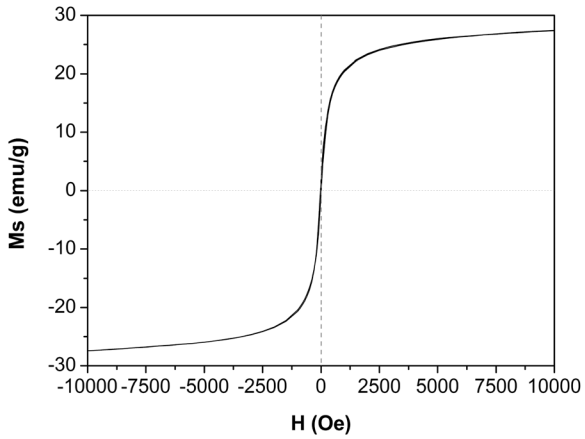

Fig. 7 Magnetic hysteresis loop of as-prepared Ag@Fe_3O_4 nanospheres at room temperature.

Inherited from the magnetic Fe_3O_4 shell, the Ag@Fe_3O_4 nanospheres exhibit typical superparamagnetic characteristics. The magnetic properties of the Ag@Fe_3O_4 nanospheres were investigated by using a superconducting quantum interference device magnetometer. From the room-temperature magnetization hysteresis loop (Fig. 7), it is found that saturated magnetization value of the core–shell Ag@Fe_3O_4 nanospheres is 27.4 emu g^{-1}. This value is lower than the hollow porous Fe_3O_4 nanospheres,[50] which may be attributed to the presence of Ag. However, it is much higher than the previously reported Fe_3O_4 based nanocatalyst.[25] Actually, with decreasing the starting [Ag^+], the M_s of the final Ag@Fe_3O_4 nanocomposite increases. (Fig. SI2†) No remnant magnetization or coercivity is found in the curve, indicating the obtained nanocomposites are superparamagnetic at room temperature. Here, the average secondary crystal size of the Fe_3O_4 shell is smaller than 20 nm (the critical value r_c) and each Fe_3O_4 nanocrystal is a single domain, thus the Fe_3O_4 shell exhibits superparamagnetic characteristics.

3.2 The parameters influencing the Ag@Fe_3O_4 nanospheres

The final core–shell Ag@Fe_3O_4 products are influenced by many factors. A series of contrastive experiments were conducted and indicated that both the concentrations of $AgNO_3$ and $Fe(NO_3)_3$ significantly affect the nanostructure of the Ag@Fe_3O_4. When the concentration of $Fe(NO_3)_3$ was fixed (5×10^{-2} mol L^{-1}), the average Ag core sizes of the product increased with increasing the Ag concentration. Fig. 8a shows a TEM image of the Ag@Fe_3O_4 products which were synthesized with a $AgNO_3$ concentration of 5.0×10^{-3} mol L^{-1}; only a 10–40 nm sized Ag core is obtained. However, when the

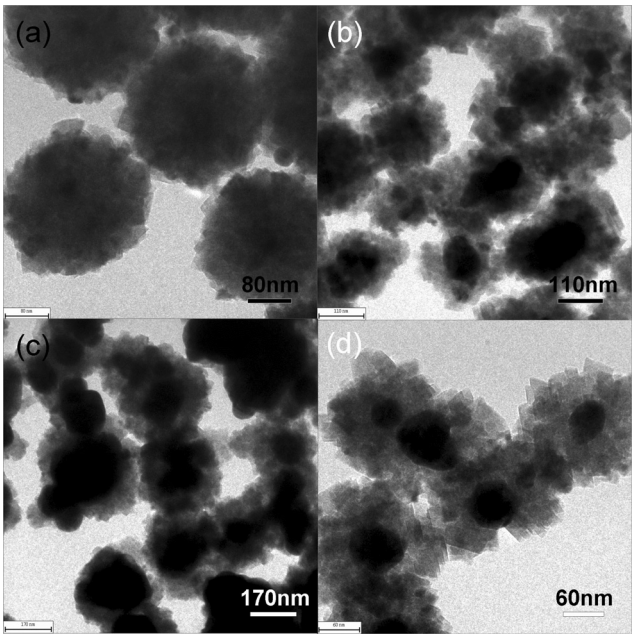

Fig. 8 TEM images of the products obtained at different concentrations of $AgNO_3$: (a) 5.0×10^{-3} mol L^{-1}, (b) 2.5×10^{-2} mol L^{-1}, the concentration of $Fe(NO_3)_3 \cdot 9H_2O$ was 5×10^{-2} mol L^{-1}; TEM images of the products obtained at different concentrations of $Fe(NO_3)_3 \cdot 9H_2O$: (c) 2.5×10^{-2} mol L^{-1}, (d) 5×10^{-2} mol L^{-1}, the concentration of $AgNO_3$ was 2.5×10^{-2} mol L^{-1}.

concentration was increased to 2.5×10^{-2} mol L^{-1}, the core size increased to 50–100 nm. Interestingly, if the concentration of $AgNO_3$ was kept a constant (2.5×10^{-2} mol L^{-1}), the size and the core size of the nanospheres decreased with increasing $[Fe^{3+}]$. Fig. 8c and d show TEM images of the $Ag@Fe_3O_4$ products under different $[Fe^{3+}]$. Clearly, the size of the products decreases from 350 to 200 nm, when the $[Fe^{3+}]$ corresponds to 2.5×10^{-2} and 5×10^{-2} mol L^{-1}, respectively. Based on the above analysis, it can be concluded that particles with tunable core size and size are successfully achieved by varying the concentrations of the precursor.

3.3 Possible mechanism for the formation of the core–shell $Ag@Fe_3O_4$ nanocomposite

To investigate the formation mechanism of the core–shell nanospheres, the detailed growth process of the $Ag@Fe_3O_4$ product was carefully followed by time-dependent experiments. Fig. 9a shows a TEM image of the sample that was synthesized after the reaction was performed for 1 h and just a gray colored precipitation was obtained. The XRD (Fig. 10) analysis indicates the as-prepared 100 nm sized nanoparticles are pure Ag. Thus the Ag core (Fig. 9a) was firstly produced at the beginning of the reaction. Due to Ag being a metal element, no specific signals are found in the FT-IR spectrum (Fig. 11). When the reaction time was increased to 3 h, a brown powder was obtained. In the XRD pattern, peaks belonging to Fe_3O_4 appeared besides the Ag peaks, which demonstrated that the Fe_3O_4 component was present in the product. In this case, a strong FT-IR absorbing

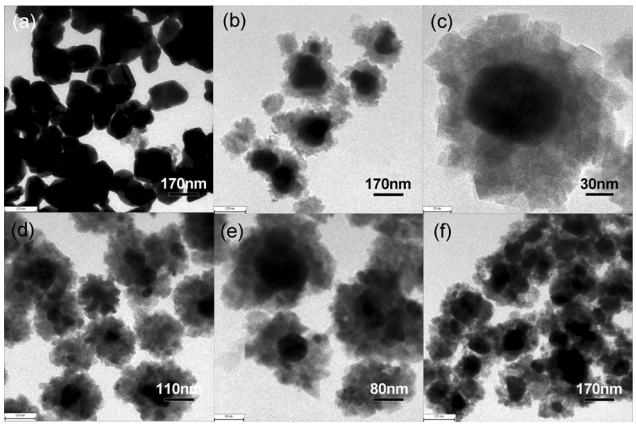

Fig. 9 TEM images of the products obtained at different reaction times: (a) 1 h, (b) 3 h, (c) 6 h, (d) 12 h, (e) 18 h, and (f) 24 h. The other conditions were the same as the typical synthesis.

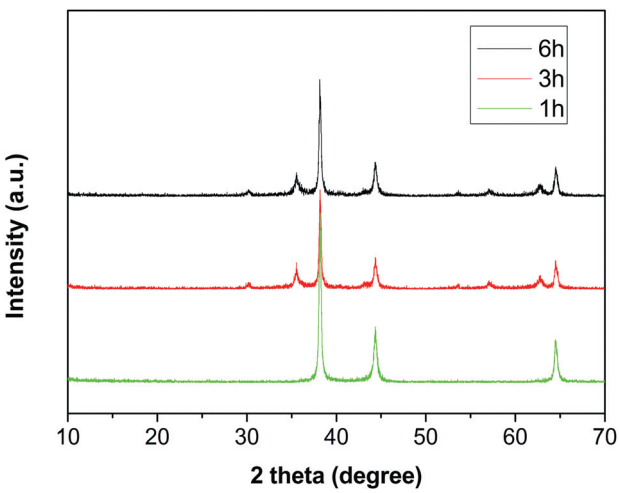

Fig. 10 XRD patterns of the products obtained at different reaction times. The other conditions were the same as the typical synthesis.

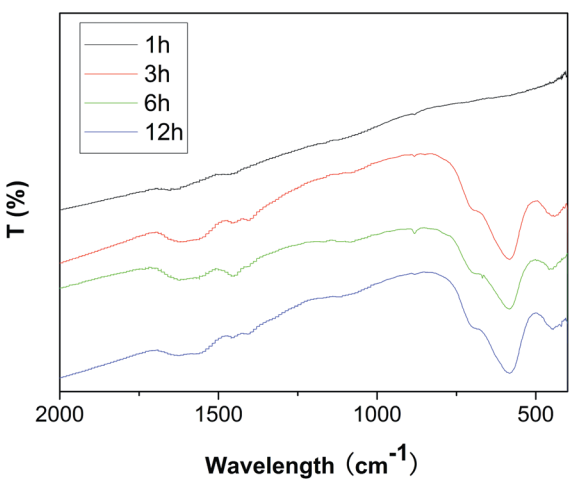

Fig. 11 FT-IR spectrum of the products obtained at different reaction times.

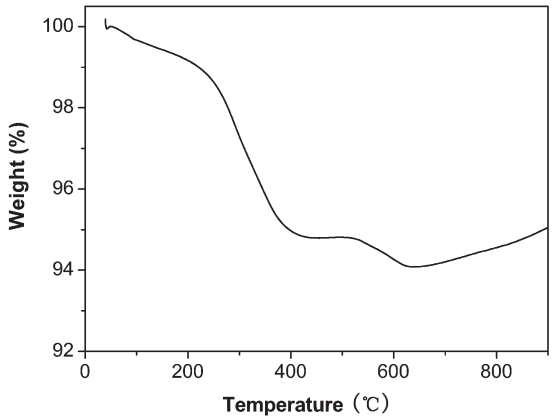

Fig. 12 TG of the as-prepared Ag@Fe_3O_4 nanospheres.

peak located at 590 cm^{-1} which was attributed to the Fe–O stretching vibration was found.[51] Fig. 9b shows a TEM image of the as-prepared sample; it can be observed that a pale shell was coated on the surface of the black core, indicating the formation of a Fe_3O_4 shell. The surface of the core–shell particle is rather rough and polyhedron like nanocrystals have not been found. Further extending the reaction time to 6 h, the crystallization of the magnetite was increased. As shown in Fig. 9c, some schistose nanostructure was found on the outermost surface of the core–shell particles and there were some pale regions at interior of the shells, suggesting the pores were achieved during this process (Fig. 9c and d). As soon as the reaction was conducted for 12 h, Ag@Fe_3O_4 nanospheres with solid core and porous shell were successfully prepared. Clearly, the Fe_3O_4 shell was composed of tiny primary nanocrystals and these nanograins were randomly packed to form the interparticle and nonordered mesopores (Fig. 9e). In comparison to the XRD pattern for the 6 h sample, the peaks for Fe_3O_4 (XRD pattern for the 12 h sample) sharply increased, indicating more crystallized Fe_3O_4 component was obtained. When the time was further increased to 18 h, the product was similar to the 12 h one except the shell of the sphere seems to be much looser (Fig. 9f). At last, when the reaction time was extended to 24 h, some yolk like nanoparticles were obtained and the porous nature was more obvious.

Fig. 11 shows a FTIR spectrum of the final Ag@Fe_3O_4 nanospheres. Besides the Fe–O stretching vibration, the peaks at 1710 and 1460 cm^{-1} are attributed to C═O and C–N vibrations, which demonstrates that there are some citrate and PAM residues presented in the core–shell nanospheres. Fig. 12 illustrates the results of the thermogravimetric analysis of the Ag@Fe_3O_4 nanospheres. The first weight loss from 100 to 250 °C belongs to the evaporation of the adsorbed water, while the weight loss at higher temperature (250–460 °C) could be attributed to the decomposition of the citrate and PAM. With further increasing the temperature, the Fe_3O_4 could transfer to Fe_2O_3 and the weight will increase. Therefore, no obvious weight loss before the temperature was higher than 530 °C was observed. The last weight loss could be due to the decomposition of the residue citrate and PAM. When the temperature increases from 630 to 900 °C, the weight also increases due to the transformation.

Based on the above analysis, a possible formation mechanism is proposed. At the beginning of the reaction, Ag particles were formed by the reaction of the Ag precursor. In the synthesis system, citrate is a reducing reagent and it is active enough to reduce the Ag^+ to form Ag nanoparticles. Due to the presence of PAM, the viscosity of the reaction system is relatively high. Thus the obtained Ag nanoparticles are stable and can be well dispersed in the solution. Moreover, the Fe^{3+}, citrate, and PAM can form a Fe-complex precursor because of the coordination and this precursor is stable within a short reaction time.[50] With increasing the reaction time, the Fe_3O_4 component was formed and it preferred to grow on the surface of the Ag core due to the surface activity. Though a uniform coating has been covered on the Ag nanoparticle to form a core–shell nanostructure, the Fe_3O_4 shell is not well crystallized and part of it is amorphous. With further increasing the reaction time, the core–shell particles experienced the Ostwald ripening process and a more crystallized Fe_3O_4 shell was obtained.[52] At last, composite particles with a single crystal Ag core and polycrystallized Fe_3O_4 shell were successfully achieved. During the ripening, the amorphous Fe_3O_4 transformed to polyhedron like nanocrystals and thus the mesopores were produced due to the loose packing of the Fe_3O_4 nanocrystals (Scheme 1). The presence of the PAM can make the Fe_3O_4 nanocrystals tightly linked with other nanocrystals to form a stable shell. Moreover, the inter-particle adherence of the Fe_3O_4 nanocrystals was reduced and thus the final Ag@Fe_3O_4 nanospheres possessed superparamagnetic characteristics.

If the starting [Ag^+] is low, the size of the as-formed Ag nanocrystals is very small and a Ag@Fe_3O_4 nanosphere with a tiny core is formed. With increasing the [Ag^+], the size of the primary Ag increases. Therefore, Ag@Fe_3O_4 nanospheres with different Ag cores can be synthesized by varying the [Ag^+]. When the [Ag^+] was kept at a constant value, the concentration of the Fe-complex increased with increasing [Fe^{3+}] and this might lead to a high viscosity. Thus the size of the Ag core decreased with increasing [Fe^{3+}], which further led to the decrement of the particle size. Therefore, the total size of the Ag@Fe_3O_4 nanosphere can also be controlled by turning the [Fe^{3+}]. Interestingly, when the [Fe^{3+}] is small enough, the Fe_3O_4 can not form an intact shell on the Ag surface and only binary structured Ag–Fe_3O_4 nanoparticles were achieved (Fig. SI1†). As a result, this facile hydrothermal method can be employed to synthesize Ag–Fe_3O_4 bi-functional nanocomposites and the shape and size of the products are controllable by varying the synthesis parameters. These nanospheres can be easily manipulated by externally applying a magnetic field, thus they could be used as bio-absorbers or catalyst carriers.

3.4 Application of Ag@Fe_3O_4 core–shell spheres for the catalytic reduction of 4-NP

The reduction of aromatic nitro compounds is commonly used for studying the catalytic performance of Ag microspheres.[53,54] Therefore, the catalytic property of the as-prepared Ag@Fe_3O_4 nanospheres was determined by using 4-NP as the substrate. After the addition of sodium borohydride into the catalytic solution, the absorption maximum of 4-NP shifts to 400 nm due to the formation of 4-nitorphenolate. Fig. 13 shows the UV/vis

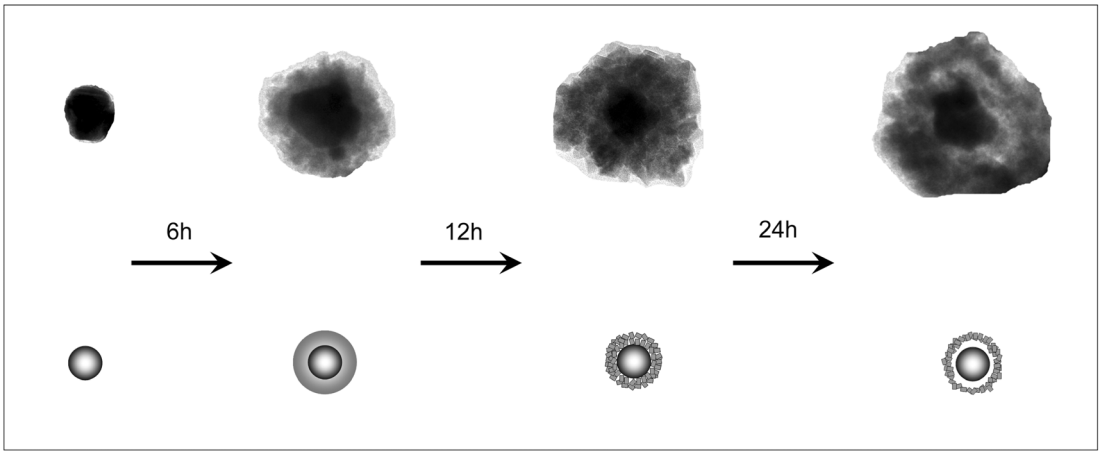

Scheme 1 A schematic illustration of the formation of the Ag@Fe_3O_4 core–shell nanospheres.

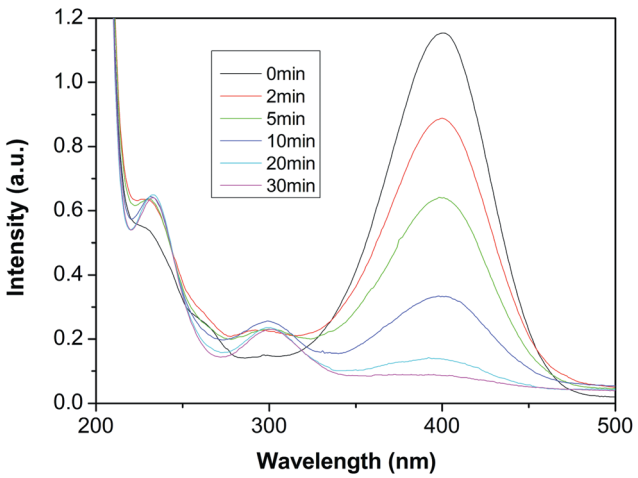

Fig. 13 UV/vis spectra of the reduction of 4-NP by adding 0.0370 mg mL^{-1} Ag@Fe_3O_4 nanospheres suspension.

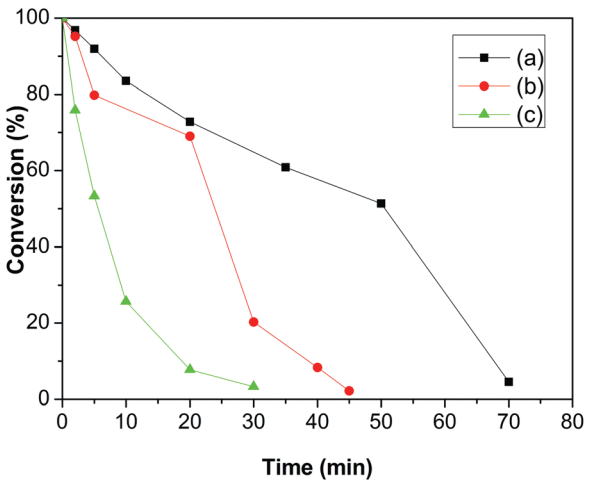

Fig. 14 Curves of conversion *vs.* time at different concentrations of the catalyst: (a) 0.0187 mg mL^{-1}, (b) 0.0262 mg mL^{-1}, (c) 0.0370 mg mL^{-1}.

absorption spectra of the reaction solution during the catalytic reductions. The maximal absorption (λ_{max} = 400 nm) of the dyes gradually decreases in time, indicating the reduction of the 4-nitorphenolate. No deactivation or poisoning of the catalyst is observed and the catalytic reduction proceeds successfully. The catalytic rate of the dyes increases with increasing the catalyst concentration. As shown in Fig. 14, the dyes can be degraded within 30, 45 and 70 min when the concentrations of the dye correspond to 0.0187, 0.0262, 0.0370 mg mL^{-1}, respectively. Moreover, the Ag@Fe_3O_4 nanospheres show superparamagnetic characteristics and they can be well dispersed into the reaction solution without quickly aggregating. After the catalytic reaction, these core–shell particles could be simply separated by applying a small magnet. Fig. 15 shows the reusability of the Ag@Fe_3O_4 nanospheres as a catalyst for the reduction of 4-NP with $NaBH_4$. It is found that after 5 recycling reactions, the 4-NP still can convert to 4-AP with the conversion rate reaching about 85%. Therefore, the as-prepared Ag@Fe_3O_4 nanospheres were proven to be a potent recyclable nanocatalyst for the industry application.

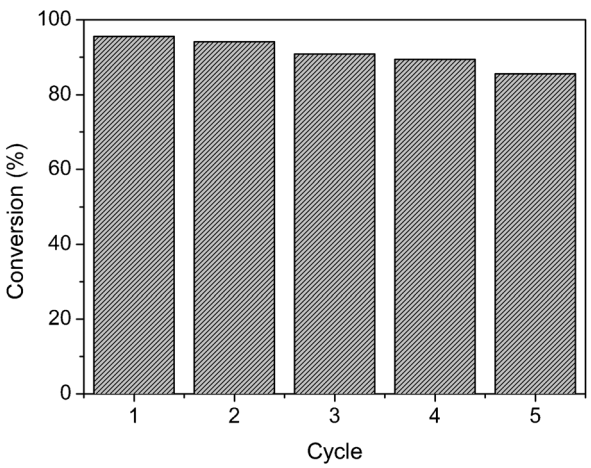

Fig. 15 The reusability of the Ag@Fe_3O_4 nanospheres as a catalyst for the reduction of 4-NP with $NaBH_4$.

4. Conclusions

In summary, we have demonstrated a facile preparation of core–shell $Ag@Fe_3O_4$ spheres by mixing $Fe(NO_3)_3$, citrate, polyacrylamide, urea and $AgNO_3$ in a mild reaction system. The shape and size of the products are controllable by varying the synthesis parameters. The time dependent experiments were constructed to investigate the synthesis procedure, which indicated the present method corresponded to an Ostwald ripening progress. The obtained core–shell $Ag@Fe_3O_4$ nanospheres can be dispersed in water and ethanol, exhibiting superparamagnetic properties and a porous shell structure. The saturated magnetization of the superparamagnetic $Ag@Fe_3O_4$ nanospheres is 27.4 emu g^{-1} at room temperature, which enable them to be recycled from the solution by simply applying a small magnet. The unique structure of core–shell $Ag@Fe_3O_4$ nanospheres can be efficiently extended to catalytic and biological applications, such as integrated imaging, targeted delivery, and photothermal therapy.

Acknowledgements

Financial support from the National Natural Science Foundation of China (Grant No. 11102202, 11072234, 11125210) and the National Basic Research Program of China (973 Program, Grant No. 2012CB937500) are gratefully acknowledged.

References

1 Y. H. Deng, D. W. Qi, C. H. Deng, X. M. Zhang and D. Y. Zhao, *J. Am. Chem. Soc.*, 2008, **130**, 28–29.
2 X. G. Peng, M. C. Schlamp, A. V. Kadavanich and A. P. Alivisatos, *J. Am. Chem. Soc.*, 1997, **119**, 7019–7029.
3 I. Alessandri, M. Zucca, M. Ferroni, E. Bontempi and L. E. Depero, *Small*, 2009, **5**, 336–340.
4 S. Alayoglu, A. U. Nilekar, M. Mavrikakis and B. Eichhorn, *Nat. Mater.*, 2008, **7**, 333–338.
5 D. B. Shenoy, A. A. Antipov, G. B. Sukhorukov and H. Möhwald, *Biomacromolecules*, 2003, **4**, 265–272.
6 P. Reiss, M. Protiere and L. Li, *Small*, 2009, **5**, 154–168.
7 H. Kim, M. Achermann, L. P. Balet, J. A. Hollingsworth and V. I. Klimov, *J. Am. Chem. Soc.*, 2005, **127**, 544–546.
8 Z. Z. Yang, Z. W. Niu, Y. F. Lu, Z. B. Hu and C. C. Han, *Angew. Chem., Int. Ed.*, 2003, **42**, 1943–1945.
9 J. M. Chan, L. F. Zhang, K. P. Yuet, G. Liao, J. W. Rhee, R. Langer and O. C. Farokhzad, *Biomaterials*, 2009, **30**, 1627–1634.
10 E. D. Smolensky, M. C. Neary, Y. Zhou, T. S. Berquo and V. C. Pierre, *Chem. Commun.*, 2011, **47**, 2149–2151.
11 S. Purushotham, P. E. J. Chang, H. Rumpel, I. H. C. Kee, R. T. H. Ng, P. K. H. Chow, C. K. Tan and R. V. Ramanujan, *Nanotechnology*, 2009, **20**, 305101.
12 H. Y. Park, M. J. Schadt, L. Wang, I. I. S. Lim, P. N. Njoki, S. H. Kim, M. Y. Jang, J. Luo and C. J. Zhong, *Langmuir*, 2007, **23**, 9050–9056.
13 X. Q. Gong, S. L. Peng, W. J. Wen, P. Sheng and W. H. Li, *Adv. Funct. Mater.*, 2009, **19**, 292–297.
14 S. H. Xuan, W. Q. Jiang and X. L. Gong, *Dalton Trans.*, 2011, **40**, 7827–7830.
15 L. Li, Y. J. Feng, Y. S. Li, W. R. Zhao and J. L. Shi, *Angew. Chem., Int. Ed.*, 2009, **48**, 5888–5892.
16 E. Taqieddin and M. Amiji, *Biomaterials*, 2004, **25**, 1937–1945.
17 D. Mariotti and R. M. Sankaran, *J. Phys. D: Appl. Phys.*, 2010, **43**, 323001.
18 I. Bica, *J. Ind. Eng. Chem.*, 2008, **14**, 230–235.
19 I. Bica, *J. Ind. Eng. Chem.*, 2009, **15**, 304–315.
20 T. A. Gad-Allah, K. Fujimura, S. Kato, S. Satokawa and T. Kojima, *J. Hazard. Mater.*, 2008, **154**, 572–577.
21 V. Polshettiwar and R. S. Varma, *Chem.–Eur. J.*, 2009, **15**, 1582–1586.
22 V. Polshettiwar and R. S. Varma, *Org. Biomol. Chem.*, 2009, **7**, 37–40.
23 S. H. Xuan, Y. X. Wang, J. C. Yu and K. C. F. Leung, *Langmuir*, 2009, **25**, 11835–11843.
24 C. S. Levin, C. Hofmann, T. A. Ali, A. T. Kelly, E. Morosan, P. Nordlander, K. H. Whitmire and N. J. Halas, *ACS Nano*, 2009, **3**, 1379–1388.
25 D. K. Yi, S. S. Lee and J. Y. Ying, *Chem. Mater.*, 2006, **18**, 2459–2461.
26 L. Y. Wang, J. Luo, Q. Fan, M. Suzuki, I. S. Suzuki, M. H. Engelhard, Y. H. Lin, N. Kim, J. Q. Wang and C. J. Zhong, *J. Phys. Chem. B*, 2005, **109**, 21593–21601.
27 M. M. Ye, Q. Zhang, Y. X. Hu, J. P. Ge, Z. D. Lu, L. He, Z. L. Chen and Y. D. Yin, *Chem. A. Eur. J.*, 2010, **16**, 6243–6250.
28 S. H. Xuan, W. Q. Jiang, X. L. Gong, Y. Hu and Z. Y. Chen, *J. Phys. Chem. C*, 2009, **113**, 553–558.
29 W. C. Huang, P. J. Tsai and Y. C. Chen, *Small*, 2009, **5**, 51–56.
30 J. S. Chen, C. P. Chen, J. Liu, R. Xu, S. Z. Qiao and X. W. Lou, *Chem. Commun.*, 2011, **47**, 2631–2633.
31 S. H. Xuan, F. Wang, X. L. Gong, S. K. Kong, J. C. Yu and K. C. F. Leung, *Chem. Commun.*, 2011, **47**, 2514–2516.
32 Q. Zhang, I. Lee, J. P. Ge, F. Zaera and Y. D. Yin, *Adv. Funct. Mater.*, 2010, **20**, 2201–2214.
33 Y. H. Deng, Y. Cai, Z. K. Sun, J. Liu, C. Liu, J. Wei, W. Li, C. Liu, Y. Wang and D. Y. Zhao, *J. Am. Chem. Soc.*, 2010, **132**, 8466–8473.
34 W. Li, Y. H. Deng, Z. X. Wu, X. F. Qian, J. P. Yang, Y. Wang, D. Gu, F. Zhang, B. Tu and D. Y. Zhao, *J. Am. Chem. Soc.*, 2011, **133**, 15830–15833.
35 R. Xu, D. S. Wang, J. T. Zhang and Y. D. Li, *Chem.–Asian J.*, 2006, **1**, 888–893.
36 F. J. Williams, D. P. C. Bird, A. Palermo, A. K. Santra and R. M. Lambert, *J. Am. Chem. Soc.*, 2004, **126**, 8509–8514.
37 J. Jiang, H. W. Gu, H. L. Shao, E. Devlin, G. C. Papaefthymiou and J. Y. Ying, *Adv. Mater.*, 2008, **20**, 4403–4407.
38 G. C. Xing, J. Jiang, J. Y. Ying and W. Ji, *Opt. Express*, 2010, **18**, 6183–6190.
39 H. B. Hu, Z. H. Wang, L. Pan, S. P. Zhao and S. Y. Zhu, *J. Phys. Chem. C*, 2010, **114**, 7738–7742.
40 D. P. Tang, R. Yuan and Y. Q. Chai, *J. Phys. Chem. B*, 2006, **110**, 11640–11646.
41 Y. Pan, J. H. Gao, B. Zhang, X. X. Zhang and B. Xu, *Langmuir*, 2010, **26**, 4184–4187.
42 D. H. Zhang, G. D. Li, J. X. Li and J. S. Chen, *Chem. Commun.*, 2008 (29), 3414–3416.
43 J. Wang, Q. W. Chen, C. Zeng and B. Y. Hou, *Adv. Mater.*, 2004, **16**, 137.
44 X. W. Liu, Q. Y. Hu, Z. Fang, Q. Wu and Q. B. Xie, *Langmuir*, 2009, **25**, 7244–7248.
45 S. H. Xuan, F. Wang, J. M. Y. Lai, K. W. Y. Sham, Y. X. J. Wang, S. F. Lee, J. C. Yu, C. H. K. Cheng and K. C. F. Leung, *ACS Appl. Mater. Interfaces*, 2011, **3**, 237–244.
46 Y. F. Zhu, W. R. Zhao, H. R. Chen and J. L. Shi, *J. Phys. Chem. C*, 2007, **111**, 5281–5285.
47 X. W. Liu, Q. Y. Hu, Z. Fang, Q. Wu and Q. B. Xie, *Langmuir*, 2009, **25**, 7244–7248.
48 L. Y. Wang, J. Bao, L. Wang, F. Zhang and Y. D. Li, *Chem.–Eur. J.*, 2006, **12**, 6341–6347.
49 L. P. Zhu, H. M. Xiao, W. D. Zhang, G. Yang and S. Y. Fu, *Cryst. Growth Des.*, 2008, **8**, 957–963.
50 W. Cheng, K. B. Tang, Y. X. Qi, J. Sheng and Z. P. Liu, *J. Mater. Chem.*, 2010, **20**, 1799–1805.
51 S. H. Xuan, L. Y. Hao, W. Q. Jiang, X. L. Gong, Y. Hu and Z. Y. Chen, *J. Magn. Magn. Mater.*, 2007, **308**, 210–213.
52 J. Li and H. C. Zeng, *Angew. Chem., Int. Ed.*, 2005, **44**, 4342–4345.
53 J. F. Huang, S. Vongehr, S. C. Tang, H. M. Lu, J. C. Shen and X. K. Meng, *Langmuir*, 2009, **25**, 11890–11896.
54 P. Liu and M. F. Zhao, *Appl. Surf. Sci.*, 2009, **255**, 3989–3993.